Article

Ionization of Decamethylmanganocene: Insights from the DFT-Assisted Laser Spectroscopy

Sergey Ketkov [1,*], Sheng-Yuan Tzeng [2], Elena Rychagova [1] and Wen-Bih Tzeng [2,*]

1   G.A. Razuvaev Institute of Organometallic Chemistry of the Russian Academy of Sciences, 49 Tropinin St., 603950 Nizhny Novgorod, Russia

2   Institute of Atomic and Molecular Sciences, Academia Sinica, 1 Section 4, Roosevelt Road, Taipei 10617, Taiwan

*   Correspondence: sketkov@iomc.ras.ru (S.K.); wbt@iams.sinica.edu.tw (W.-B.T.)

Abstract: Metallocenes represent one of the most important classes of organometallics with wide prospects for practical use in various fields of chemistry, materials science, molecular electronics, and biomedicine. Many applications of these metal complexes are based on their ability to form molecular ions. We report the first results concerning the changes in the molecular and electronic structure of decamethylmanganocene, Cp^*_2Mn, upon ionization provided by the high-resolution mass-analyzed threshold ionization (MATI) spectroscopy supported by DFT calculations. The precise ionization energy of Cp^*_2Mn is determined as 5.349 ± 0.001 eV. The DFT modeling of the MATI spectrum shows that the main structural deformations accompanying the detachment of an electron consist in the elongation of the Mn-C bonds and a change in the Me out-of-plane bending angles. Surprisingly, the DFT calculations predict that most of the reduction in electron density (ED) upon ionization is associated with the hydrogen atoms of the substituents, despite the metal character of the ionized orbital. However, the ED difference isosurfaces reveal a complex mechanism of the charge redistribution involving also the carbon atoms of the molecule.

Keywords: metallocenes; ionization energy; laser spectroscopy; DFT calculations; electron density

1. Introduction

In 2022, chemists celebrate the 70th anniversary of the first publications on a unique sandwich structure of ferrocene, Cp_2Fe ($Cp = \eta^5\text{-}C_5H_5$) [1,2]. With the discovery of this iconic metal complex, a new era of organometallic chemistry has started. Currently, metallocenes are of ever-increasing interest among researchers in fundamental and applied science, since they are relevant to the modern theories of metal–ligand bonding [3–6], electro- and magnetochemistry [7–13], metallopolymers [14–18], biomedicine [19–22], catalysis [23–25], nanoelectronics [26–32] and molecular machines [33–35]. Many applications of metallocenes take advantage of their pronounced reducing properties, which allow for the easy formation of stable or reactive sandwich ions [7–10,14–16,23–30,33–39]. These properties are associated with the low ionization energies, *I*, corresponding to the detachment of an electron from a sandwich high occupied molecular orbital (MO) with substantial metal *d* character [40–47]. Comprehensive studies of ionization processes in metallocenes are, therefore, especially important for understanding their reactivity.

Unprecedented opportunities for studying the details of the ionization of molecules appeared with the development of high-resolution methods using laser irradiation. Precise measurements of ionization energies are provided by the zero kinetic energy (ZEKE) or mass-analyzed threshold ionization (MATI) spectroscopy [48,49] using the laser excitation of molecules to high Rydberg levels (so-called ZEKE states) which are then ionized by an electric pulse. The ZEKE states of polyatomic molecules with high *I* values are usually populated by multiphoton laser excitation through intermediate vibronic levels. For organometallics, this approach encounters experimental difficulties associated with poor

resolution of vibronic states and fast photodissociation of the excited molecules [50,51]. However, the ZEKE states of metallocenes and related sandwich complexes with $I < 6$ eV can be populated in a one-photon experiment using standard laser sources.

Nevertheless, the experimental measurement of the MATI and ZEKE spectra of sandwich compounds remains a nontrivial task due to the low volatility and thermal stability of these metal complexes as well as their air and moisture sensitivity. Among metallocenes, the MATI spectrum has so far been recorded only for Cp_2Co [52]. The MATI/ZEKE data have been obtained also for some bisarene complexes [53–65] and few mixed sandwiches [66]. These studies demonstrated new possibilities provided by the MATI and ZEKE techniques for detecting substituent effects and structural changes of sandwich molecules upon ionization [67]. In the present work, we report the first MATI spectrum of jet-cooled decamethylmanganocene, Cp^*_2Mn ($Cp^* = \eta^5\text{-}C_5Me_5$). The manganocene-methylated derivatives are of particular fundamental interest, since the introduction of the CH_3 groups to the Cp rings of Cp_2Mn leads to a "switching" of the ground electronic state from the $^6A_1$ sextet to the $^2E_2$ doublet [40,68–73] (we use the irreducible representations of the D_5 point group for designation of the electronic states and MOs). In contrast to many other metallocenes, manganocene does not form stable cationic derivatives. On the other hand, its permethylated low-spin analogue, Cp^*_2Mn, is readily oxidized to yield the $Cp^*_2Mn^+$ cation [11,73]. Such systems can display properties of bulk molecular ferromagnets [74,75]. Therefore, the details of structural and energetic changes accompanying the ionization of Cp^*_2Mn attract special attention. Our combined MATI/DFT study provides new insights into these details.

2. Results and Discussion

Similar to other theoretical studies of metallocenes [72,76–79], our B3PW91/6-311++ G(d,p) DFT calculations show that high-energy occupied MOs of Cp^*_2Mn have a predominantly metal d character (Figure 1). The electronic configurations of the $Cp^*_2Mn^0$ neutral and the $Cp^*_2Mn^+$ cation are . . . $(d_{x^2\text{-}y^2})^1(d_{z^2})^2(d_{xy})^2$ and . . . $(d_{x^2\text{-}y^2})^1(d_{z^2})^1(d_{xy})^2$, respectively. These configurations correspond to the $^2E_2$ doublet ground state of the D_5 neutral and the $^3E_2$ triplet ground state of the ion [40,71]. However, the degeneracy of MO $d_{x^2\text{-}y^2}$ and d_{xy}, which would take place in the D_5 point group, is actually lifted in Cp^*_2Mn (Figure 1) due to the Jahn–Teller (JT) distortion.
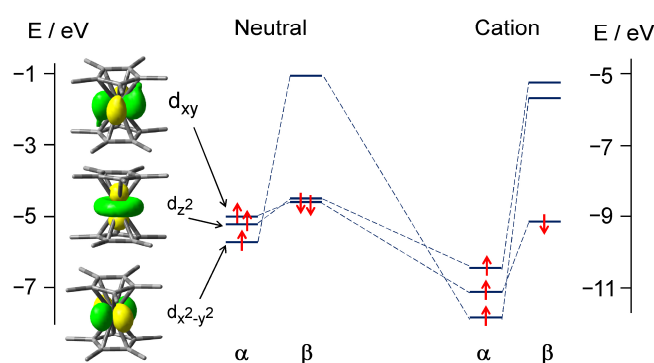

Figure 1. MO correlation diagram of the $Cp^*_2Mn^0$ neutral and $Cp^*_2Mn^+$ cation. The MO isosurfaces are given for the wavefunction value of 0.04. Notice the different energy scales for $Cp^*_2Mn^0$ (left) and $Cp^*_2Mn^+$ (right).

The ground-state $^3E_2$ $Cp^*_2Mn^+$ cation is formed by a detachment of the non-bonding d_{z^2} β-electron from the neutral molecule. The I value can be determined in a laser ionization experiment by recording the photoionization efficiency (PIE) curve or, much more accurately, by measuring the MATI spectrum.

2.1. PIE and MATI Spectra of Cp*$_2$Mn

The PIE curve of Cp*$_2$Mn (Figure 2a) shows a rather sharp step in the 43,000–43,200 cm^{-1} region corresponding to the ionization energy of 5.33–5.36 eV, which agrees very well with the I = 5.33 $\pm$ 0.10 eV value determined earlier from the "classical" photoelectron spectrum [71]. The MATI spectrum of Cp*$_2$Mn (Figure 2b) reveals a clearly defined peak arising from a detachment of an electron from the ZEKE levels lying a few wavenumbers below the cation ground vibronic state. The I value of 43,146 $\pm$ 8 cm^{-1}, or 5.349 $\pm$ 0.001 eV, corresponds to a narrow MATI signal descend range. Therefore, the MATI spectrum of Cp*$_2$Mn provides an extremely accurate ionization energy, the error being two orders of magnitude smaller than that of standard photoelectron spectroscopy.
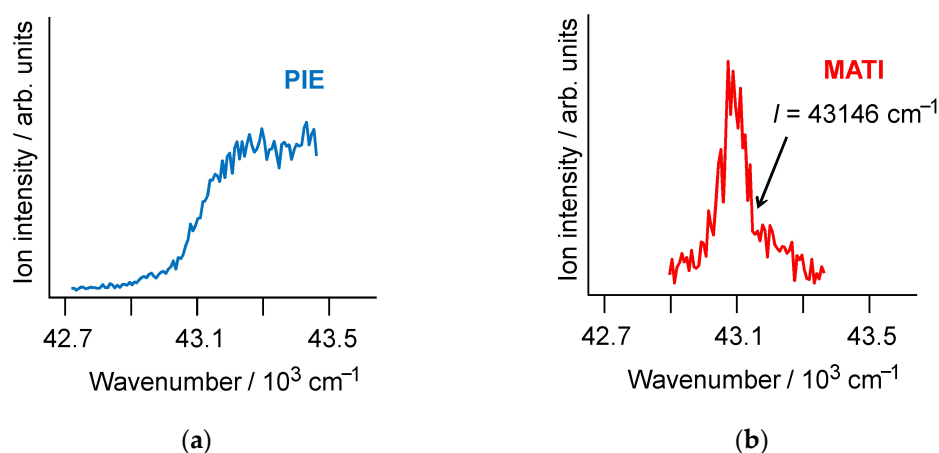
Figure 2. The PIE (**a**) and MATI (**b**) spectra of jet-cooled Cp*$_2$Mn. The ionization energy (I) corresponds to the narrow range of the MATI signal descend.

The precise I value of Cp*$_2$Mn obtained from the MATI spectrum provides new accurate information on the difference between the Mn-Cp* bond dissociation energies in the decamethylmanganocene cation and neutral [67]:

$$D(\text{Cp*}_2\text{Mn}^+) - D(\text{Cp*}_2\text{Mn}^0) = I(\text{Mn}^0) - I(\text{Cp*}_2\text{Mn}^0), \tag{1}$$

where $D(\text{Cp*}_2\text{Mn}^{+/0})$ corresponds to the energy change in the reaction:

$$\text{Cp*}_2\text{Mn}^{+/0} \rightarrow \text{Mn}^{+/0} + 2\text{C}_5\text{Me}_5{}^\bullet. \tag{2}$$

Taking into account the known ionization energy of the manganese atom, $I(\text{Mn}^0)$ = 4.43402 eV [80], and the $I(\text{Cp*}_2\text{Mn}^0)$ value derived from our MATI spectrum we obtain the dissociation energy difference (Equation (1)) as 2.085 $\pm$ 0.001 eV, or 201.2 $\pm$ 0.1 kJ mol^{-1}. Therefore, the mean Mn-Cp* bond dissociation energy in the decamethylmanganocene cation, equal to 0.5 $D(\text{Cp*}_2\text{Mn}^+)$, is 100.6 kJ mol^{-1} larger than that in the neutral molecule. The accuracy in the determination of this difference from the MATI data presented in this work (0.1 kJ mol^{-1}) is much better than that obtained from the UV photoelectron spectrum of Cp*$_2$Mn [71] (ca. 10 kJ mol^{-1}). As a result, the use of laser threshold ionization spectroscopy provides new possibilities for studying fine substituent effects in manganocenes, similar to those found for bisarene sandwich systems [67].

The MATI spectrum of Cp*$_2$Mn (Figure 2b) reveals no lower-energy vibronic features accompanying the strong peak with the maximum at 43,100 cm^{-1}. Therefore, this peak corresponds to the origin (the 0_0^0 transition between the ground vibrational states of Cp*$_2$Mn^0 and Cp*$_2$Mn$^+$). Then, the vertical and adiabatic ionization energies of Cp*$_2$Mn coincide. A different situation holds with the MATI spectrum of Cp$_2$Co [51], where the vertical I value is 0.115 eV higher than the adiabatic ionization energy. This difference can be associated with the antibonding nature of the ionized MO in Cp$_2$Co [40,51,77].

On the other hand, the chromium bisarene complexes with the non-bonding d_{z^2} electron ionized produce MATI spectra [52–56,58,64–66] showing the 0_0^0 vibronic component as the strongest feature like Cp*$_2$Mn. The vibrationally resolved high-resolution MATI spectra provide much more information on the sandwich molecules than structureless "classical" photoelectron spectra or PIE curves.

2.2. Vibronic Structure of the Cp*$_2$Mn MATI Spectrum

Detailed analysis of the Cp*$_2$Mn MATI spectrum recorded at a higher concentration of the organometallic molecules in the supersonic jet reveals the weaker high-energy vibronic components accompanying the origin (Figure 3a). Their assignment can be made on the basis of the DFT modeling. The B3PW91/6-311++G(d,p) simulation (Figure 3b) gives a MATI vibronic structure that agrees very well with the experiment. The relative positions of the vibronic components (Table 1) correspond to the vibrational frequencies of the free Cp*$_2$Mn$^+$ cation. Only two normal vibrations of Cp*$_2$Mn$^+$ are responsible for the MATI features of noticeable intensity (Figure 3). They are denoted in this work as ν_1 and ν_2. According to the DFT calculations, the 130 cm^{-1} ν_1 mode corresponds to the Me out-of-plane bend, while the 352 cm^{-1} ν_2 vibration represents the symmetric Mn-ring stretch without displacement of the methyl carbon nuclei. Both the ν_1 and ν_2 modes involve the change of the Mn-C$_{ring}$-C$_{Me}$ angle. The relative atomic shifts for the ν_1 and ν_2 vibrations are shown in Figure 4, and the corresponding animations are presented in the Supplementary Materials (Videos S1 and S2).
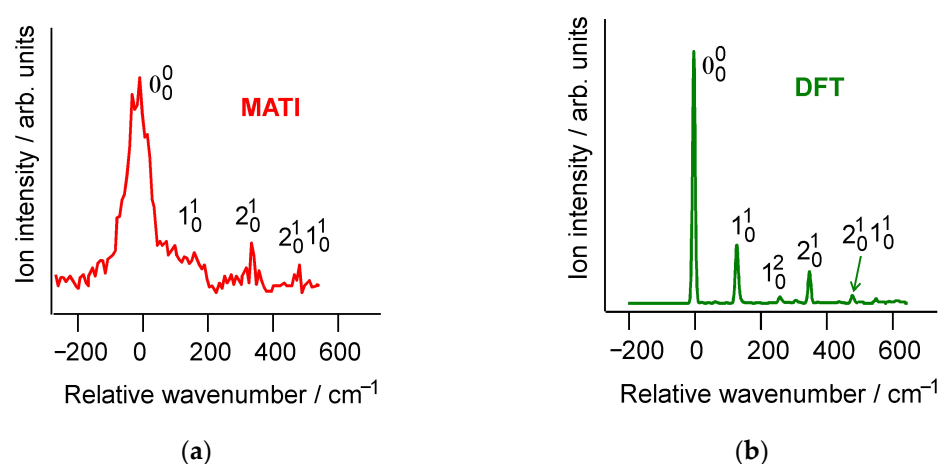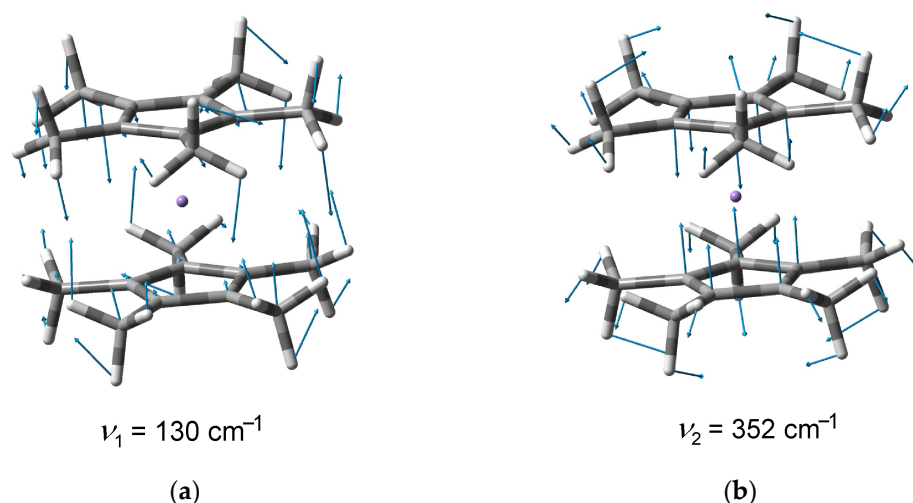

Figure 3. The experimental (**a**) and DFT-simulated (**b**) vibronic structure of the Cp*$_2$Mn MATI spectrum.

Table 1. Relative positions (cm^{-1}) of the vibronic components in the Cp*$_2$Mn experimental MATI spectrum and its DFT simulation.

Vibronic Component [a]	MATI	DFT
0_{0^0}	0	0
1_{0^1}	140 [b]	130
1_{0^2}	-	261
2_{0^1}	340	352
$2_{0^1}1_{0^1}$	480	482

[a] The vibronic transitions are notated as $N_{v''v'}$, where N is the vibration number and v'' and v' are the vibrational quantum number in the neutral and ionic state, respectively. [b] Shoulder.

$\nu_1 = 130\ cm^{-1}$ $\nu_2 = 352\ cm^{-1}$

(**a**)   (**b**)

Figure 4. Relative atomic shifts corresponding to the ν_1 (**a**) and ν_2 (**b**) vibrations of the Cp*$_2$Mn$^+$ cation.

Both ν_1 and ν_2 would be totally symmetric modes in a D_5 decamethylmetallocene molecule like closed-shell Cp*$_2$Fe. The experimental and simulated MATI spectra of Cp*$_2$Mn (Figure 3) do not contain vibronic components that could be associated with the JT distortion of the neutral or cationic species in the degenerate E_2 electronic state. This testifies for similar shifts of the Cp*$_2$Mn^0 and Cp*$_2$Mn$^+$ molecular geometries from the D_5 point group along the JT active vibrational coordinates. The good agreement between the experimental and simulated MATI vibronic structure (Figure 3, Table 1) shows that the B3PW91/6-311++G(d,p) level of DFT provides reliable information about the structural changes in Cp*$_2$Mn upon ionization.

2.3. Changes in the Geometry of Decamethylmanganocene upon Ionization

The structural transformations accompanying ionization of Cp*$_2$Mn can be analyzed on the basis of the neutral and ion geometries obtained from the X-ray diffraction experiments [68,74]. However, in this case the changes caused by the intramolecular effects would be superimposed on those resulted from the intermolecular and cation–anion interactions. The Cp*$_2$Mn structure in the gas phase has been determined by electron diffraction [69], but these data provide only averaged geometry of the sandwich molecule corresponding to the high symmetry of the D_{5d} point group. Therefore, the DFT calculations verified by the simulation of the experimental gas-phase MATI spectrum would be preferable as a basis for studying the fine details of the structural changes accompanying ionization of the Cp*$_2$Mn molecule.

The atom numbering as well as selected bond lengths and angles in one Cp*Mn fragment are given in Figures 5 and 6. The atomic coordinates are provided in the Supplementary Materials (Tables S1 and S2). The geometry of the other fragment is identical since the molecule with a staggered conformation of the Cp* ligands possesses a center of inversion. The optimized staggered geometry of Cp*$_2$Mn^0 is in accord with the X-ray structure [68,81] (Tables S3 and S4, see the Supplementary Materials). The calculated interatomic distances in Cp*$_2$Mn^0 (Figure 5a) agree well with the single-crystal X-ray diffraction data [68] (r(C-C) = 1.409–1.434 Å for the carbocycle and r(Mn-C) = 2.105–2.118 Å) and gas-phase electron diffraction results [69] (1.440 and 2.130 Å, respectively). The DFT-based structural parameters of the Cp*$_2$Mn$^+$ ion (Figure 5b) also correlate with the crystal structure [74], though the experimental solid-phase parameters depend strongly on the counter ion.
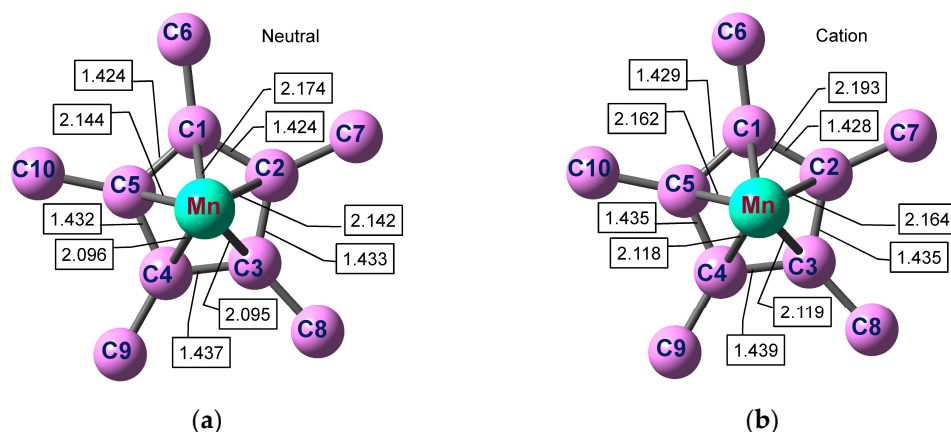
Figure 5. Mn-C(ring) and C(ring)-C(ring) distances (Å) in the optimized Cp*$_2$Mn^0 neutral (**a**) and Cp*$_2$Mn$^+$ cation (**b**). The hydrogen atoms are omitted for clarity.
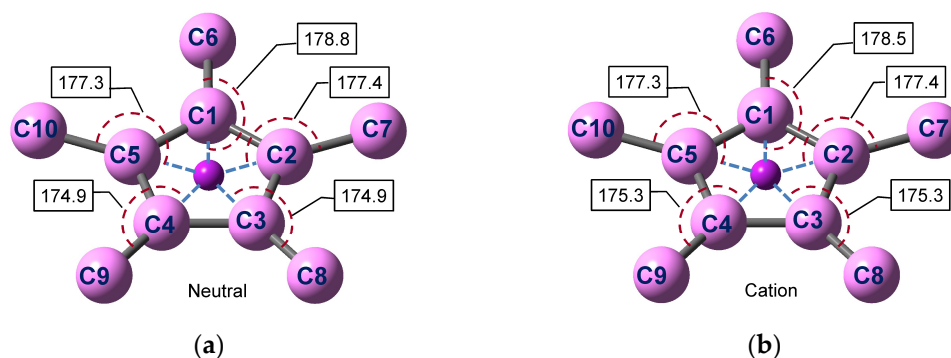
Figure 6. Centroid(ring)-C(ring)-C(Me) angles in the optimized Cp*$_2$Mn^0 neutral (**a**) and Cp*$_2$Mn$^+$ cation (**b**). The hydrogen atoms are omitted for clarity.

The optimized structure of the neutral Cp*$_2$Mn molecule or the corresponding cation is nearly symmetric relative to the MnC1C6 plane. Together with the inversion center at the Mn atom, this means that the molecular symmetry is close to the C_{2h} point group. The deviation from the ideal D_{5d} symmetry is caused by the JT distortion of the Cp*$_2$Mn neutral or ion in the degenerate E_2 ground electronic state. The JT distortion in both Cp*$_2$Mn^0 and Cp*$_2$Mn$^+$ includes mainly: (1) a slippage of the Cp* ligands leading to a shift of the Mn atom projection on the ring plane from the ring centroid and to different Mn-C bond lengths; (2) an in-plane ring deformation (a contraction of the C1-C2 and C1-C5 bonds, an elongation of the C3-C4 bond); (3) unequal bending of the methyl groups away from the metal atom (the C8 and C9 atoms lie at the longest distance from the ring plane). The first and the second trend were also revealed by the X-ray study [68].

It should be noticed that the JT distortion of Cp*$_2$Mn^0 differs from that in Cp$_2$Co^0 where the Cp rings become non-planar [51,82]. This difference arises from the different nature of the single-occupied MO in these sandwich molecules. In Cp*$_2$Mn^0, the unpaired electron occupies MO $d_{x^2-y^2}$ belonging to the e_2 set in a non-distorted molecule. In Cp$_2$Co^0, the single-occupied MO is derived from the Co 3d$_{xz}$ or 3d$_{yz}$ and Cp $\pi(e_1)$ wavefunctions.

The structural transformation of Cp*$_2$Mn^0 upon ionization consists mainly in lengthening the Mn-Cp* distances and changing the Me bending angles (Table 2). As a result of the electron detachment, the distance between the ligand ring planes increases by 0.048 Å, from 3.494 Å to 3.542 Å. This increase in the ligand–ligand distance exceeds that computed earlier for (η^6-C$_6$H$_6$)$_2$Cr (0.038 Å [66]). The symmetry of the Cp*$_2$Mn^0 neutral and Cp*$_2$Mn$^+$ ion is the same, so only totally symmetric vibrations ν_1 and ν_2 corresponding to the Me bend and Mn-Cp* stretch, respectively, are excited in the MATI experiment. In contrast to decamethylmanganocene, ionization of cobaltocene leads to the highly symmet-

ric closed-shell Cp_2Co^+ ion. Accordingly, the MATI spectrum of Cp_2Co reveals the e_2 and e_1 vibrational modes which are active in the JT effect and pseudo-JT effect occurring in the neutral molecule [51,83]. The ionized MO of $Cp*_2Mn^0$ represents an almost "pure" $3d_{z^2}$ orbital of the Mn atom (Figure 1). However, the electron density (ED) analysis reveals a much more complex charge redistribution upon ionization of decamethylmanganocene than would be expected from the simple subtraction of the d_{z^2} ED.

Table 2. Calculated changes in selected bond lengths and atom-plane(ring) distances Δr (Å) as well as angles $\Delta\phi$ (°) upon ionization of $Cp*_2Mn^0$.

Distance	Δr	Angle	$\Delta\phi$
C1-C2	0.004	Mn-centroid(ring)-C1	−0.1
C2-C3	0.002	Mn-centroid(ring)-C2	0.0
C3-C4	0.002	Mn-centroid(ring)-C3	0.1
Mn-C1	0.019	Mn-C1-C6	0.1
Mn-C2	0.022	Mn-C2-C7	−0.3
Mn-C3	0.024	Mn-C3-C8	−0.7
C6-plane(ring)	0.009	centroid(ring)-C1-C6	−0.3
C7-plane(ring)	0.001	centroid(ring)-C2-C7	−0.1
C8-plane(ring)	−0.012	centroid(ring)-C3-C8	0.6
Mn-plane(ring)	0.024		

2.4. Charge Density Redistribution after Electron Detachment from $Cp*_2Mn^0$

The ED difference (EDD) isosurfaces (Figure 7) corresponding to the ED change on going from $Cp*_2Mn^0$ to $Cp*_2Mn^+$ at the geometry of the neutral (the vertical ionization) reveal areas of both a decrease and an increase in the ED. The ED gain near the metal is the result of charge transfer from the Cp* ligands to the Mn atom during ED relaxation after ionization. The 0.005 a.u. EDD isosurface (Figure 7a) shows the ED loss arising from the detachment of the Mn d_{z^2} electron and from the consequent transfer of the ligand π-electron density to the Mn atom. The largest area of the positive EDD visualizes the acquisition of ED by the metal atom through the $Mn(d_{xz,yz})/Cp(\pi)$ e_1-occupied orbital. A smaller ED shift from C(Me) to C(ring) along the C-C σ-bonds is also observed (Figure 7a). The 0.003 a.u. and 0.001 EDD isosurfaces (Figure 7b) reveal an additional ED loss by the H atoms of the Me groups accompanied by a ED increase near C(Me) around the C-H bonds. The positive EDD region appears inside the carbocycles near the C-C σ-bonds.

| (**a**) | (**b**) | (**c**) |
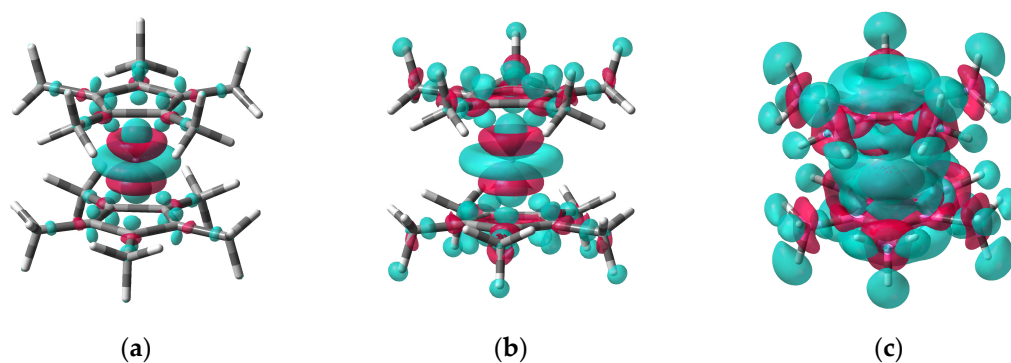
Figure 7. Isosurfaces of the electron density difference between the $Cp*_2Mn^+$ cation and neutral $Cp*_2Mn^0$ at the optimized geometry of the latter (vertical ionization of $Cp*_2Mn$). The isovalues are 0.005 a.u. (**a**), 0.003 a.u. (**b**) and 0.001 a.u. (**c**). The blue and red colors correspond to the loss and gain of ED, respectively.

The inhomogeneous ED redistribution upon ionization of decamethylmanganocene leads to nontrivial changes in the atomic charges. They were calculated in this work by integration of the ED over the atomic basins within the frames of the Quantum Theory of

Atoms in Molecules (QTAIM) [84,85]. Due to the transfer of the ED from the ligands to the metal, after the removal of the d_{z^2} electron, the Mn charge increases by only 0.198 a.u. on going from $Cp^*_2Mn^0$ to $Cp^*_2Mn^+$ (Table 3). Correspondingly, each Cp^* ligand becomes less negative by 0.401 a.u. However, the carbon charges change very little (Table 3). Moreover, the C atoms of both carbocycles and methyl groups become more negative upon ionization of $Cp^*_2Mn^0$. The total change in the C(ring) and C(Me) charges in the molecule is -0.044 and -0.037 a.u., respectively. The loss of the ED by the ligands is provided, therefore, entirely by the hydrogen atoms of the methyl groups. Indeed, the total increase of the H positive charges is 0.883 a.u. It is worth mentioning that the larger charge shift (0.044 a.u.) corresponds to the H atoms oriented away from the metal (Table 3). This agrees well with the EDD isosurfaces (Figure 7b,c) which demonstrate, however, that, despite the decisive role of H atoms in the total loss of the ED by the ligands during $Cp^*_2Mn^0$ ionization, carbon atoms are also involved in the ED redistribution mechanism. The loss of the π-electron density by the carbocyles, which transfer a negative charge to the metal, is compensated by the ED gain through the C(ring)-C(Me) σ-bonds.

Table 3. Charges q (a.u.) on selected atoms [a] and fragments in the optimized $Cp^*_2Mn^0$ neutral and $Cp^*_2Mn^+$ cation and their change upon ionization Δq.

Atom or Fragment	q (Neutral)	q (Cation)	Δq
Mn	0.874	1.072	0.198
C1	-0.103	-0.105	-0.002
C2	-0.114	-0.118	-0.004
C3	-0.123	-0.129	-0.006
C6	0.000	-0.003	-0.003
C7	0.003	-0.001	-0.004
C8	0.005	0.001	-0.004
H(C6) [b]	0.006	0.050	0.044
H(C6) [c]	0.005	0.028	0.023
H(C6) [c]	0.006	0.029	0.023
H(C7) [b]	0.009	0.053	0.044
H(C7) [c]	0.007	0.029	0.022
H(C7) [c]	0.008	0.031	0.023
H(C8) [b]	0.012	0.056	0.044
H(C8) [c]	0.009	0.031	0.022
H(C8) [c]	0.010	0.032	0.022
Me(C6)	0.023	0.108	0.085
Me(C7)	0.027	0.112	0.085
Me(C8)	0.032	0.116	0.084
Cp^*	-0.437	-0.036	0.401

[a] See the text and Figures 5 and 6 for the atom numbering; the carbon atoms of the methyl groups are indicated in parentheses. [b] The H atoms oriented away from the metal. [c] The H atoms oriented towards the metal.

3. Materials and Methods

3.1. PIE and MATI Experiments

Decamethylmanganocene was purchased from Alfa Aesar and purified by sublimation in the PIE and MATI experiments. All manipulations with the air- and moisture-sensitive compound were carried out under an inert atmosphere in a glovebox. The MATI setup was described earlier [64,86]. The Cp^*_2Mn sample was placed into a stainless steel tube heated up to 170–180 °C. The sublimed vapor-phase organometallics diluted with helium (1.5 bar) was expanded into an evacuated chamber using a heated pulsed valve. The molecular beam selected by a skimmer was directed into a high-vacuum (10^{-8} Torr) ionization chamber where the Cp^*_2Mn neutrals were excited (MATI) or ionized (PIE) by the UV laser radiation. Tunable laser pulses in the 225–235 nm region were formed when doubling the dye-laser frequency (Lambda-Physik, Scanmate UV) by the BBO-I crystal. The Nd:YAG laser (Quanta-Ray PRO-190-10) was used for the pumping of the dye laser. The laser wavelengths were calibrated with a wavemeter (Coherent, WaveMaster). In the PIE experiment, the molecular

ions formed by ionization of Cp*$_2$Mn were detected by a microchannel plate particle detector of the time-of-flight mass spectrometer. The photoionization mass spectrum revealed an intense molecular ion signal at *m/z* = 325 a.u. (C$_{20}$H$_{30}$Mn$^+$). The ion signal at variable laser wavelengths was collected and analyzed. In the MATI experiment, the neutrals were excited by a UV laser pulse to the long-lived ZEKE states. To remove the prompt ions, a pulsed electric field of ~1 V/cm was switched on about 20 ns after the laser pulses. Then, another pulse of the +200 V/cm electric field was applied with a 11 μs delay to ionize the ZEKE-state molecules. The obtained Cp*$_2$Mn$^+$ ions were detected and analyzed like those in the PIE measurements.

3.2. DFT Calculations and Electron Density Analysis

The geometries of the neutral and cationic decamethylmanganocene were optimized at the B3PW91/6-311++G(d,p) level of DFT. The combination of the hybrid B3PW91 functional [87,88] and triple-ζ split valence basis set 6-311++G(d,p) including diffuse and polarization functions on hydrogen and the heavy atoms [89,90] demonstrated earlier good performance when modeling the MATI spectra of bisarene complexes [64,65] and mixed sandwiches [66]. The experimental X-ray structure [68] was used as a starting geometry in the optimization procedure. Harmonic vibrational frequencies were calculated and the results were used to compute the Franck-Condon factors and produce the model MATI spectra. No imaginary frequencies were found. The calculations were carried out with the Gaussian 16 program package [91]. The QT AIM analysis of the ED distribution was performed with the AIM ALL suite [92]. The atomic charges were obtained by integration of ED over the atomic basins using the Promega1 algorithm [93]. The EDD isosurfaces were built as a result of the neutral ED subtraction from the ion ED at the ground-state geometry using the Multiwfn code [94].

4. Conclusions

The high-resolution MATI spectroscopy provides unprecedented accuracy in determination of the ionization energy of decamethylmanganocene. The *I* value of 43,146 $\pm$ 8 cm^{-1}, or 5.349 $\pm$ 0.001 eV is obtained on the basis of the Cp*$_2$Mn MATI spectrum. The adiabatic and vertical ionization energies of Cp*$_2$Mn coincide. The precise *I* value makes it possible to determine with high accuracy the difference between the Mn-Cp* mean bond energies in the Cp*$_2$Mn$^+$ cation and Cp*$_2$Mn^0 neutral (100.6 $\pm$ 0.1 kJ mol^{-1}). The bond strengthening in the cation can be associated with a weaker repulsion between the less negative Cp* ligands and stronger Mn-Cp* covalent interactions that resulted from the increase in the d$_{xz,yz}$ electron density. The B3PW91/6-311++G(d,p) model of the MATI vibronic structure agrees very well with the experiment. Although the geometry of both Cp*$_2$Mn^0 and Cp*$_2$Mn$^+$ is distorted because of the JT effect, only the symmetric Cp*-Mn-Cp* stretching vibration and Mn-C(ring)-C(Me) bending mode are detected in the MATI structure. Correspondingly, the main structural deformations accompanying the electron detachment include an elongation of the Mn-C bonds and changes in the Me out-of-plane bending angle. Interestingly, atomic charge calculations using the QTAIM method predict that the largest part of the reduction in ED during ionization is associated with substituent hydrogen atoms, despite the metallic nature of the ionized orbital. The ED difference isosurfaces reveal, however, a complex mechanism of the charge redistribution involving also the carbon atoms of the molecule. Thus, DFT-assisted MATI spectroscopy represents a powerful instrument that unveils the details of the structural and electronic transformations accompanying ionization of the permethylated metallocene molecule.

Supplementary Materials: The following supporting information can be downloaded at: https://www.mdpi.com/article/10.3390/molecules27196226/s1, Table S1: Atomic coordinates of the optimized Cp*$_2$Mn^0 molecule; Table S2: Atomic coordinates of the optimized Cp*$_2$Mn$^+$ cation; Table S3: Calculated and experimental selected bond lengths in the Cp*$_2$Mn^0 molecule; Table S4: Calculated and experimental selected bond angles in the Cp*$_2$Mn^0 molecule; Video S1: Animated ν$_1$

vibration of Cp*$_2$Mn$^+$; Video S2: Animated ν_2 vibration of Cp*$_2$Mn$^+$. References [68,81] are cited in the supplementary materials.

Author Contributions: Conceptualization, S.K.; methodology, S.K. and W.-B.T.; formal analysis, E.R. and S.-Y.T.; investigation, S.-Y.T.; writing—original draft preparation, S.K.; writing—review and editing, W.-B.T. All authors have read and agreed to the published version of the manuscript.

Institutional Review Board Statement: Not applicable.

Informed Consent Statement: Not applicable.

Data Availability Statement: The data reported in this study are available in the present article and in the Supplementary Materials.

Conflicts of Interest: The authors declare no conflict of interest.

Sample Availability: The sample of Cp*$_2$Mn is available from commercial sources.

References

1. Wilkinson, G.; Rosenblum, M.; Whiting, M.C.; Woodward, R.B. The Structure of Iron Bis-Cyclopentadienyl. *J. Am. Chem. Soc.* **1952**, *74*, 2125–2126. [CrossRef]
2. Fischer, E.O.; Pfab, W. Cyclopentadien-Metallkomplexe, Ein Neuer Typ Metallorganischer Verbindungen. *Z. Naturforsch.* **1952**, *7*, 377–379. [CrossRef]
3. Elschenbroich, C. *Organometallics*, 3rd ed.; Wiley-VCH: Weinheim, Germany, 2006; pp. 528–549.
4. Frenking, G. Chemical Bonding in Transition Metal Compounds. In *The Chemical Bond: Chemical Bonding across the Periodic Table*; Frenking, G., Shaik, S., Eds.; Wiley-VCH: Berlin/Weinheim, Germany, 2014; Chapter 7; pp. 175–217.
5. Cloke, F.G.N.; Green, J.C.; Kilpatrick, A.F.R.; O'Hare, D. Bonding in Pentalene Complexes and Their Recent Applications. *Coord. Chem. Rev.* **2017**, *344*, 238–262. [CrossRef]
6. Gritzner, G. Reference Redox Systems in Nonaqueous Systems and the Relation of Electrode Potentials in Nonaqueous and Mixed Solvents to Standard Potentials in Water. In *Handbook of Reference Electrodes*; Inzelt, G., Lewenstam, A., Scholz, F., Eds.; Springer: Berlin/Heidelberg, Germany, 2013; Chapter 2; pp. 25–31. [CrossRef]
7. Jörissen, J.; Speiser, B. Preparative Electrolysis on the Laboratory Scale. In *Organic Electrochemistry: Revised and Expanded*, 5th ed.; Hammerich, O., Speiser, B., Eds.; CRC Press: Boca Raton, FL, USA, 2015; Chapter 7; pp. 263–330. [CrossRef]
8. Ding, Y.; Zhang, C.; Zhang, L.; Zhou, Y.; Yu, G. Molecular Engineering of Organic Electroactive Materials for Redox Flow Batteries. *Chem. Soc. Rev.* **2018**, *47*, 69–103. [CrossRef] [PubMed]
9. Liu, K.; Liu, Y.; Lin, D.; Pei, A.; Cui, Y. Materials for Lithium-Ion Battery Safety. *Sci. Adv.* **2018**, *4*, eaas9820. [CrossRef]
10. Yee, G.T.; Miller, J.S. Metallocene-Based Magnets. In *Magnetism: Molecules to Materials V*; Miller, J.S., Drillon, M., Eds.; Wiley-VCH: Weinheim, Germany, 2005; Chapter 7; pp. 223–260.
11. Cirera, J.; Ruiz, E. Electronic and Steric Control of the Spin-Crossover Behavior in [(Cp^R)$_2$Mn] Manganocenes. *Inorg. Chem.* **2018**, *57*, 702–709. [CrossRef]
12. Shuku, Y.; Hirai, Y.; Semenov, N.A.; Kadilenko, E.; Gritsan, N.P.; Zibarev, A.V.; Rakitin, O.A.; Awaga, K. 3D Molecular Network And Magnetic Ordering, Formed By Multi-Dentate Magnetic Couplers, Bis(Benzene)Chromium(I) and [1,2,5]Thiadiazolo[3,4-*c*][1,2,5]Thiadiazolidyl. *Dalton Trans.* **2018**, *47*, 9897–9902. [CrossRef]
13. Ormaza, M.; Abufager, P.; Verlhac, B.; Bachellier, N.; Bocquet, M.-L.; Lorente, N.; Limot, L. Controlled Spin Switching in a Metallocene Molecular Junction. *Nat. Commun.* **2017**, *8*, 1974. [CrossRef]
14. Braunschweig, H.; Damme, A.; Demeshko, S.; Dück, K.; Kramer, T.; Krummenacher, I.; Meyer, F.; Radacki, K.; Stellwag-Konertz, S.; Whittell, G.R. A Paramagnetic Heterobimetallic Polymer: Synthesis, Reactivity, and Ring-Opening Polymerization of Tin-Bridged Homo- and Heteroleptic Vanadoarenophanes. *J. Am. Chem. Soc.* **2015**, *137*, 1492–1500. [CrossRef]
15. Musgrave, R.A.; Russell, A.D.; Hayward, D.W.; Whittell, G.R.; Lawrence, P.G.; Gates, P.J.; Green, J.C.; Manners, I. Main-chain Metallopolymers at the Static–Dynamic Boundary Based on Nickelocene. *Nat. Chem.* **2017**, *9*, 743–750. [CrossRef]
16. Astruc, D. Why is Ferrocene so Exceptional? *Eur. J. Inorg. Chem.* **2017**, *2017*, 6–29. [CrossRef]
17. Eloi, J.-C.; Chabanne, L.; Whittell, G.R.; Manners, I. Metallopolymers with Emerging Applications. *Mater. Today* **2008**, *11*, 28–36. [CrossRef]
18. Wang, Y.; Astruc, D.; Abd-El-Aziz, A.S. Metallopolymers for Advanced Sustainable Applications. *Chem. Soc. Rev.* **2019**, *48*, 558–636. [CrossRef] [PubMed]
19. Van Staveren, D.R.; Metzler-Nolte, N. Bioorganometallic Chemistry of Ferrocene. *Chem. Rev.* **2004**, *104*, 5931–5986. [CrossRef]

20. Ihara, T. Oranometallic Complexes for Biosensing. In *Advances in Bioorganometallic Chemistry*, 1st ed.; Hirao, T., Moriuchi, T., Eds.; Elsevier: Amsterdam, The Netherlands, 2019; Chapter 14; pp. 277–303.

21. Patra, M.; Gasser, G. The medicinal chemistry of ferrocene and its derivatives. *Nat. Rev. Chem.* **2017**, *1*, 0066. [CrossRef]

22. Albada, B.; Metzler-Nolte, N. Organometallic–Peptide Bioconjugates: Synthetic Strategies and Medicinal Applications. *Chem. Rev.* **2016**, *116*, 11797–11839. [CrossRef]

23. Astruc, D. *Organometallic Chemistry and Catalysis*; Springer: Berlin/Heidelberg, Germany, 2007; pp. 251–288.

24. Collins, S.; Linnolahti, M. Activation of Substituted Metallocene Catalysts Using Methylaluminoxane. *ChemCatChem* **2022**, *14*, e202101918. [CrossRef]

25. Bochmann, M. *Organometallics and Catalysis: An Introduction*; Oxford University Press: Oxford, UK, 2015; 432p.

26. Liu, R.; Ke, S.-H.; Baranger, H.U.; Yang, W. Organometallic Spintronics: Dicobaltocene Switch. *Nano Lett.* **2005**, *5*, 1959–1962. [CrossRef]

27. Engtrakul, C.; Sita, L.R. Ferrocene-Based Nanoelectronics: Regioselective Syntheses and Electrochemical Characterization of α-Monothiol and α,ω-Dithiol, Phenylethynyl-Conjugated, 2,5-Diethynylpyridyl- and Pyridinium-Linked Diferrocene Frameworks Having an End-to-End Distance of $\sim$4 nm. *Organometallics* **2008**, *27*, 927–937. [CrossRef]

28. Morari, C.; Rungger, I.; Rocha, A.R.; Sanvito, S.; Melinte, S.; Rignanese, G.-M. Electronic Transport Properties of 1,1′-Ferrocene Dicarboxylic Acid Linked to Al(111) Electrodes. *ACS Nano* **2009**, *3*, 4137–4143. [CrossRef]

29. Lawson, B.; Zahl, P.; Hybertsen, M.S.; Kamenetska, M. Formation and Evolution of Metallocene Single-Molecule Circuits with Direct Gold-π Links. *J. Am. Chem. Soc.* **2022**, *144*, 6504–6515. [CrossRef] [PubMed]

30. Inkpen, M.S.; White, A.J.P.; Albrecht, T.; Long, N.J. Avoiding Problem Reactions at the Ferrocenyl-Alkyne Motif: A Convenient Synthesis of Model, Redox-Active Complexes for Molecular Electronics. *Dalton Trans.* **2014**, *43*, 15287–15290. [CrossRef]

31. Wilson, L.E.; Hassenrück, C.; Winter, R.F.; White, A.J.P.; Albrecht, T.; Long, N.J. Ferrocene- and Biferrocene-Containing Macrocycles towards Single-Molecule Electronics. *Angew. Chem. Int. Ed. Engl.* **2017**, *56*, 6838–6842. [CrossRef]

32. Ghosh, A.; Mishra, S.; Giri, S.; Mobin, S.M.; Bera, A.; Chatterjee, S. Electrolyte-Free Dye-Sensitized Solar Cell with High Open Circuit Voltage Using a Bifunctional Ferrocene-Based Cyanovinyl Molecule as Dye and Redox Couple. *Organometallics* **2018**, *37*, 1999–2002. [CrossRef]

33. Scottwell, S.O.; Elliott, A.B.S.; Shaffer, K.J.; Nafady, A.; McAdam, C.J.; Gordon, K.C.; Crowley, J.D. Chemically and Electrochemically Induced Expansion and Contraction of a Ferrocene Rotor. *Chem. Commun.* **2015**, *51*, 8161–8164. [CrossRef] [PubMed]

34. Scottwell, S.O.; Crowley, J.D. Ferrocene-Containing Non-Interlocked Molecular Machines. *Chem. Commun.* **2016**, *52*, 2451–2464. [CrossRef]

35. Scottwell, S.O.; Barnsley, J.E.; McAdam, C.J.; Gordon, K.C.; Crowley, J.D. A Ferrocene Based Switchable Molecular Folding Ruler. *Chem. Commun.* **2017**, *53*, 7628–7631. [CrossRef]

36. Tritto, I.; Sacchi, M.C.; Locatelli, P.; Li, S.X. Metallocene ion pairs: A direct insight into the reaction equilibria and polymerization by 13C NMR spectroscopy. *Macromol. Symp.* **1995**, *89*, 289–298. [CrossRef]

37. Abel, E.W.; Stone, F.G.A.; Wilkinson, G. *Comprehensive Organometallic Chemistry II: A Review of the Literature 1982–1994*, 1st ed.; Pergamon: Oxford, UK, 1995; Volume 5–9.

38. Deck, P.A.; Marks, T.J. Cationic Metallocene Olefin Polymerization Catalysts. Thermodynamic and Kinetic Parameters for Ion Pair Formation, Dissociation, and Reorganization. *J. Am. Chem. Soc.* **1995**, *117*, 6128–6129. [CrossRef]

39. Bochmann, M. Cationic Group 4 Metallocene Complexes and Their Role in Polymerisation Catalysis: The Chemistry of Well Defined Ziegler Catalysts. *J. Chem. Soc. Dalton Trans.* **1996**, *3*, 255–270. [CrossRef]

40. Green, J.C. Gas Phase Photoelectron Spectra of *d*- and *f*-Block Organometallic Compounds. *Struct. Bond.* **1981**, *43*, 37–112.

41. Rabalais, J.W.; Werme, L.O.; Bergmark, T.; Karlsson, L.; Hussain, M.; Siegbahn, K. Electron Spectroscopy of Open-Shell Systems: Spectra of $Ni(C_5H_5)_2$, $Fe(C_5H_5)_2$, $Mn(C_5H_5)_2$, and $Cr(C_5H_5)_2$. *J. Chem. Phys.* **1972**, *57*, 1185–1192. [CrossRef]

42. Green, J.C.; Green, M.L.H.; Kaltsoyannis, N.; Mountford, P.; Scott, P.; Simpson, S.J. Synthesis and Electronic and Molecular Structures Of η-Cycloheptatrienyl η-Cyclopentadienyl Derivatives of Vanadium, Niobium, and Tantalum: Photoelectron Spectroscopic, Electrochemical, and X-Ray Crystallographic Study. *Organometallics* **1992**, *11*, 3353–3361. [CrossRef]

43. Ketkov, S.Y.; Domrachev, G.A. Rydberg Transitions in the Near-Ultraviolet Vapor-Phase Absorption Spectra of 3d Metallocenes. *Inorg. Chim. Acta* **1990**, *178*, 233–242. [CrossRef]

44. Ketkov, S.Y. Photoabsorption Study of Electronic Excited States of (η^5-Cyclopentadienyl)(η^6-Arene)Manganese. *J. Organomet. Chem.* **1994**, *465*, 225–231. [CrossRef]

45. Révész, A.; Szepes, L.; Baer, T.; Sztáray, B.J. Binding Energies and Isomerization in Metallocene Ions from Threshold Photoelectron Photoion Coincidence Spectroscopy. *J. Am. Chem. Soc.* **2010**, *132*, 17795–17803. [CrossRef]

46. Green, J.C. Periodic Trends Revealed by Photoelectron Studies of Transition Metal and Lanthanide Compounds. *Struct. Bond.* **2019**, *181*, 81–110. [CrossRef]

47. Green, J.C.; Decleva, P. Photoionization cross-sections: A guide to electronic structure. *Coord. Chem. Rev.* **2005**, *249*, 209–228. [CrossRef]

48. Schlag, E.W. *ZEKE Spectroscopy*; Cambridge University Press: Cambridge, UK, 1998; 277p.

49. Yang, D.-S. Photoelectron spectra of metal-containing molecules with resolutions better than 1 meV. *Coord. Chem. Rev.* **2001**, *214*, 187–213. [CrossRef]

50. Clara, M.; Neusser, H.J. Ultrafast Dissociation Dynamics of Ferrocene and [3]-Ferrocenophan. *J. Phys. Chem. A* **2001**, *105*, 5577–5585. [CrossRef]

51. Ketkov, S.Y.; Selzle, H.L. Threshold Ionization of Cobaltocene: The Metallocene Molecule Revealing Zero Kinetic Energy States. *Angew. Chem. Int. Ed.* **2012**, *51*, 11527–11530. [CrossRef] [PubMed]

52. Ketkov, S.Y.; Selzle, H.L.; Schlag, E.W. Study of Jet-Cooled Bis(η^6-Benzene)Chromium by Multiphoton Zero Kinetic Energy–Mass-Analyzed Threshold Ionization Spectroscopy. *Isr. J. Chem.* **2004**, *44*, 65–69. [CrossRef]

53. Ketkov, S.Y.; Selzle, H.L.; Schlag, E.W. High-Resolution Mass-Analyzed Threshold Ionization Study of Deuterated Derivatives of Bis(η^6-Benzene)Chromium. *Organometallics* **2006**, *25*, 1712–1716. [CrossRef]

54. Choi, K.-W.; Choi, S.; Baek, S.J.; Kim, S.K. Pulsed-Field Ionization Spectroscopy of High Rydberg States (n = 50–200) of Bis(η^6-Benzene)Chromium. *J. Chem. Phys.* **2007**, *126*, 034308. [CrossRef]

55. Ketkov, S.Y.; Selzle, H.L.; Schlag, E.W. Nanosecond Multiphoton Ionization Spectroscopy of Transition-Metal Sandwich Compounds: A Comparative Study of Nickelocene, Ferrocene and Bis(η^6-Benzene)Chromium. *Mol. Phys.* **2004**, *102*, 1749–1757. [CrossRef]

56. Choi, K.-W.; Kim, S.K.; Ahn, D.-S.; Lee, S. One-Photon Mass-Analyzed Threshold Ionization Spectroscopy of Bis(η^6-Benzene)Chromium and Its Benzene and Ar Clusters. *J. Phys. Chem. A* **2004**, *108*, 11292–11295. [CrossRef]

57. Sohnlein, B.R.; Yang, D.-S. Pulsed-Field Ionization Electron Spectroscopy of Group 6 Metal (Cr, Mo, and W) Bis(Benzene) Sandwich Complexes. *J. Chem. Phys.* **2006**, *124*, 134305. [CrossRef]

58. Ketkov, S.Y.; Selzle, H.L.; Cloke, F.G.N. Direct Detection of Individual Bis(arene) Rotational Isomers in the Gas Phase by Mass-Analyzed Threshold Ionization Spectroscopy. *Angew. Chem. Int. Ed.* **2007**, *46*, 7072–7074. [CrossRef]

59. Sohnlein, B.R.; Lei, Y.; Yang, D.-S. Electronic States of Neutral and Cationic Bis(Benzene) Titanium and Vanadium Sandwich Complexes Studied by Pulsed Field Ionization Electron Spectroscopy. *J. Chem. Phys.* **2007**, *127*, 114302. [CrossRef]

60. Lee, J.S.; Kumari, S.; Yang, D.-S. Conformational Isomers and Isomerization of Group 6 (Cr, Mo, and W) Metal-Bis(Toluene) Sandwich Complexes Probed by Variable-Temperature Electron Spectroscopy. *J. Phys. Chem. A.* **2010**, *114*, 11277–11284. [CrossRef]

61. Ketkov, S.Y.; Selzle, H.L.; Cloke, F.G.N.; Markin, G.V.; Schevelev, Y.A.; Domrachev, G.A.; Schlag, E.W. Zero Kinetic Energy Spectroscopy: Mass-Analyzed Threshold Ionization Spectra of Chromium Sandwich Complexes with Alkylbenzenes, (η^6-RPh)$_2$Cr (R = Me, Et, *i*-Pr, *t*-Bu). *J. Phys. Chem. A* **2010**, *114*, 11298–11303. [CrossRef] [PubMed]

62. Yang, D.-S. High-Resolution Electron Spectroscopy of Gas-Phase Metal−Aromatic Complexes. *J. Phys. Chem. Lett.* **2011**, *2*, 25–33. [CrossRef] [PubMed]

63. Kumari, S.; Yang, D.-S. High-Resolution Electron Spectroscopy and Rotational Conformers of Group 6 Metal (Cr, Mo, and W) Bis(mesitylene) Sandwich Complexes. *J. Phys. Chem. A* **2013**, *117*, 13336–13344. [CrossRef] [PubMed]

64. Ketkov, S.Y.; Markin, G.V.; Tzeng, S.-Y.; Tzeng, W.-B. Fine Substituent Effects in Sandwich Complexes: A Threshold Ionization Study of Monosubstituted Chromium Bisarene Compounds. *Chem. Eur. J.* **2016**, *22*, 4690–4694. [CrossRef]

65. Ketkov, S.Y.; Tzeng, S.-Y.; Wu, P.-Y.; Markin, G.V.; Tzeng, W.-B. DFT Supported Threshold Ionization Study of Chromium Biphenyl Complexes: Unveiling the Mechanisms of Substituent Influence on Redox Properties of Sandwich Compounds. *Chem. Eur. J.* **2017**, *23*, 13669–13675. [CrossRef]

66. Ketkov, S.Y.; Tzeng, S.-Y.; Rychagova, E.A.; Markin, G.V.; Makarov, S.G.; Tzeng, W.-B. Laser Spectroscopic and Computational Insights into Unexpected Structural Behaviours of Sandwich Complexes on Ionization. *Dalton Trans.* **2021**, *50*, 10729–10736. [CrossRef]

67. Ketkov, S.Y. Substituent Effects on the Electronic Structures of Sandwich Compounds: New Understandings Provided By DFT-Assisted Laser Ionization Spectroscopy of Bisarene Complexes. *Dalton Trans.* **2020**, *49*, 569–577. [CrossRef]

68. Freyberg, D.P.; Robbins, J.L.; Raymond, K.N.; Smart, J.C. Crystal and Molecular Structures of Decamethylmanganocene and Decamethylferrocene. Static Jahn-Teller Distortion in a Metallocene. *J. Am. Chem. Soc.* **1979**, *101*, 892–897. [CrossRef]

69. Fernholt, L.; Haaland, A.; Seip, R.; Robbins, J.L.; Smart, J.C. The Molecular Structure of Decamethylmanganocene, [η-C$_5$(CH$_3$)$_5$]$_2$Mn, Determined by Gas Phase Electron Diffraction. *J. Organomet. Chem.* **1980**, *194*, 351–355. [CrossRef]

70. Walter, M.D.; Sofield, C.D.; Booth, C.H.; Andersen, R.A. Spin Equilibria in Monomeric Manganocenes: Solid-State Magnetic and EXAFS Studies. *Organometallics* **2009**, *28*, 2005–2019. [CrossRef]

71. Cauletti, C.; Green, J.C.; Kelly, M.R.; Powell, P.; van Tilborg, J.; Robbins, J.; Smart, J. Photoelectron Spectra of Metallocenes. *J. Electr. Spectrosc. Rel. Phenom.* **1980**, *19*, 327–353. [CrossRef]

72. Wang, G.; Slebodnick, C.; Butcher, R.J.; Tam, M.C.; Crawford, T.D.; Yee, G.T. A Family of Decamethylmetallocene Charge-Transfer Salt Magnets Using Methyl Tricyanoethylenecarboxylate (MTCE) as the Electron Acceptor. *J. Am. Chem. Soc.* **2004**, *126*, 16890–16895. [CrossRef]

73. Robbins, J.L.; Edelstein, N.M.; Cooper, S.R.; Smart, J.C. Syntheses and Electronic Structures of Decamethylmanganocenes. *J. Am. Chem. Soc.* **1979**, *101*, 3853–3857. [CrossRef]

74. Faulmann, C.; Riviere, E.; Dorbes, S.; Senocq, F.; Coronado, E.; Cassoux, P. Ferromagnetism in [Mn(Cp*)$_2$]$^+$-Derived Complexes: The "Miraculous" Stacking in [Mn(Cp*)$_2$][Ni(dmit)$_2$]. *Eur. J. Inorg. Chem.* **2003**, *2003*, 2880–2888. [CrossRef]

75. Broderick, W.E.; Thompson, J.A.; Day, E.P.; Hoffman, B.M. A Molecular Ferromagnet with a Curie Temperature of 6.2 Kelvin: [Mn(C$_5$(CH$_3$)$_5$)$_2$]$^+$[TCNQ]$^-$. *Science* **1990**, *249*, 401–403. [CrossRef]

76. Clack, D.W.; Warren, K.D. Metal-Ligand Bonding in 3 d Sandwich Complexes. *Struct. Bond.* **1980**, *39*, 1–41. [CrossRef]

77. Xu, Z.-F.; Xie, Y.; Feng, W.-L.; Schaefer, H.F. Systematic Investigation of Electronic and Molecular Structures for the First Transition Metal Series Metallocenes M(C_5H_5)$_2$ (M = V, Cr, Mn, Fe, Co, and Ni). *J. Phys. Chem. A* **2003**, *107*, 2716–2729. [CrossRef]

78. Matsuzawa, N.; Seto, J.; Dixon, D.A. Density Functional Theory Predictions of Second-Order Hyperpolarizabilities of Metallocenes. *J. Phys. Chem. A* **1997**, *101*, 9391–9398. [CrossRef]

79. Hrobárik, P.; Reviakine, R.; Arbuznikov, A.V.; Malkina, O.L.; Malkin, V.G.; Köhler, F.H.; Kaupp, M. Density Functional Calculations of NMR Shielding Tensors for Paramagnetic Systems with Arbitrary Spin Multiplicity: Validation On 3d Metallocenes. *J. Chem. Phys.* **2007**, *126*, 024107. [CrossRef]

80. Lias, S.G.; Bartmess, J.E.; Liebman, J.F.; Holmes, J.L.; Levin, R.D.; Mallard, W.G. Ion Energetics Data. In *NIST Chemistry WebBook, NIST Standard Reference Database Number 69*; Linstrom, P.J., Mallard, W.G., Eds.; National Institute of Standards and Technology: Gaithersburg, MD, USA, 2022. [CrossRef]

81. Augart, N.; Boese, R.; Schmid, G. Phasenübergang von Decamethylmanganocen. *Z. Anorg. Allg. Chem.* **1991**, *595*, 27–34. [CrossRef]

82. Zlatar, M.; Schläpfer, C.-W.; Fowe, E.P.; Daul, C. Density Functional Theory Study of the Jahn-Teller Effect in Cobaltocene. *Pure Appl. Chem.* **2009**, *81*, 1397–1411. [CrossRef]

83. Ketkov, S.Y.; Rychagova, E.A.; Zhigulin, G.Y.; Tzeng, S.Y.; Tzeng, W.B. Quantum-Chemical Modeling of the Mass-Analyzed Threshold Ionization Spectra of Ferrocene and Cobaltocene. *High Energ. Chem.* **2020**, *54*, 414–420. [CrossRef]

84. Bader, R.F.W. *Atoms in Molecules: A Quantum Theory*; Oxford University Press: Oxford, UK, 1990; 438p.

85. Cortés-Guzmán, F.; Bader, R.F.W. Complementarity of QTAIM and MO theory in the study of bonding in donor-acceptor complexes. *Coord. Chem. Rev.* **2005**, *249*, 633–662. [CrossRef]

86. Xu, Y.; Tzeng, S.Y.; Shivatare, V.; Takahashi, K.; Zhang, B.; Tzeng, W.B. Identification of Four Rotamers of *M*-Methoxystyrene by Resonant Two-Photon Ionization and Mass Analyzed Threshold Ionization Spectroscopy. *J. Chem. Phys.* **2015**, *142*, 124314. [CrossRef] [PubMed]

87. Becke, A.D. Density-Functional Thermochemistry. III. The Role of Exact Exchange. *J. Chem. Phys.* **1993**, *98*, 5648–5652. [CrossRef]

88. Perdew, J.P.; Burke, K.; Wang, Y. Generalized Gradient Approximation for the Exchange-Correlation Hole of a Many-Electron System. *Phys. Rev. B Condens. Matter* **1996**, *54*, 16533–16539. [CrossRef]

89. Krishnan, R.; Binkley, J.S.; Seeger, R.; Pople, J.A. Self-Consistent Molecular Orbital Methods. XX. A Basis Set for Correlated Wave Functions. *J. Chem. Phys.* **1980**, *72*, 650–654. [CrossRef]

90. Clark, T.; Chandrasekhar, J.; Spitznagel, G.W.; Schleyer, P.v.R. Efficient Diffuse Function-Augmented Basis Sets for Anion Calculations. III. The 3-21+G Basis Set for First-Row Elements, Li-F. *J. Comput. Chem.* **1983**, *4*, 294–301. [CrossRef]

91. Frisch, M.J.; Trucks, G.W.; Schlegel, H.B.; Scuseria, G.E.; Robb, M.A.; Cheeseman, J.R.; Scalmani, G.; Barone, V.; Petersson, G.A.; Nakatsuji, H.; et al. *Gaussian 16*; Gaussian, Inc.: Wallingford, CT, USA, 2016.

92. Keith, T.A. *AIMAll*, Version 13.05.06; TK Gristmill Software: Overland Park, KS, USA, 2013. Available online: https://aim.tkgristmill.com (accessed on 20 September 2015).

93. Lu, T.; Chen, F. Multiwfn: A Multifunctional Wavefunction Analyzer. *J. Comput. Chem.* **2012**, *33*, 580–592. [CrossRef]

94. Lu, T.; Chen, F. Quantitative Analysis of Molecular Surface Based on Improved Marching Tetrahedra Algorithm. *J. Mol. Graph. Model.* **2012**, *38*, 314–323. [CrossRef]